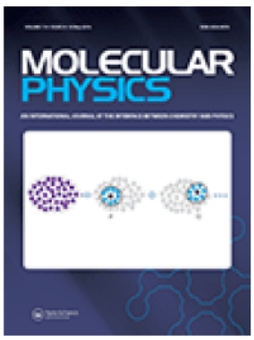

Taylor & Francis
Taylor & Francis Group

Molecular Physics

An International Journal at the Interface Between Chemistry and Physics

ISSN: 0026-8976 (Print) 1362-3028 (Online) Journal homepage: https://www.tandfonline.com/loi/tmph20

Shape-controlled crystallisation pathways in dense fluids of *ccp*-forming hard polyhedra

Richmond S. Newman, Samanthule Nola, Julia Dshemuchadse & Sharon C. Glotzer

To cite this article: Richmond S. Newman, Samanthule Nola, Julia Dshemuchadse & Sharon C. Glotzer (2019): Shape-controlled crystallisation pathways in dense fluids of *ccp*-forming hard polyhedra, Molecular Physics, DOI: 10.1080/00268976.2019.1668574

To link to this article: https://doi.org/10.1080/00268976.2019.1668574

MOLECULAR PHYSICS
https://doi.org/10.1080/00268976.2019.1668574

Taylor & Francis
Taylor & Francis Group

CUMMINGS SPECIAL ISSUE

Shape-controlled crystallisation pathways in dense fluids of *ccp*-forming hard polyhedra

Richmond S. Newman[a,*], Samanthule Nola[b,*], Julia Dshemuchadse[a] and Sharon C. Glotzer[a,b,c,d]

[a]Department of Chemical Engineering, University of Michigan, Ann Arbor, MI, USA; [b]Macromolecular Science and Engineering Program, University of Michigan, Ann Arbor, MI, USA; [c]Department of Materials Science and Engineering, University of Michigan, Ann Arbor, MI, USA; [d]Biointerfaces Institute, University of Michigan, Ann Arbor, MI, USA

ABSTRACT

Emergent directional entropic forces that favour facet-to-facet alignment of neighbouring colloidal particles – arising from multi-body interactions upon crowding – should cause the process by which colloidal crystals form from fluids of hard polyhedra to be different than that from fluids of hard spheres. We compute nucleation-free energy barriers for a family of shapes that all self-assemble the same cubic close-packed (*ccp*) crystal structure formed by hard spheres and find that changing rhombicuboctahedra into rhombic dodecahedra by successively removing facets that compete with the *ccp* structure cause a systematic decrease in barrier heights. We show that this decrease arises from the increased prominence of facets aligned with neighbouring shapes in the target crystal, which produce local environments in the fluid that facilitate crystallisation.

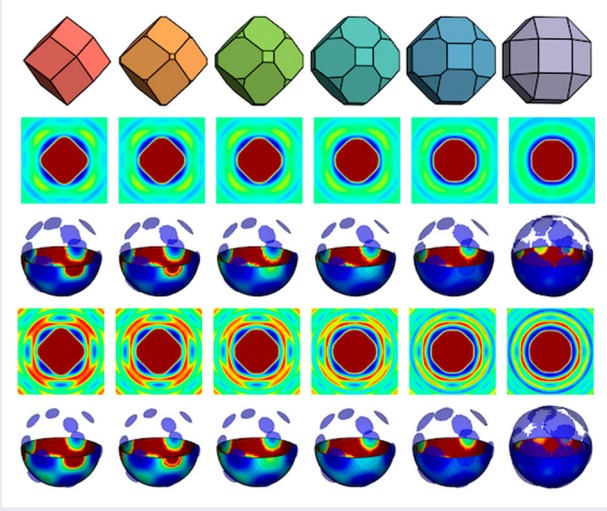

ARTICLE HISTORY
Received 1 June 2019
Accepted 5 September 2019

KEYWORDS
Crystallisation; hard shapes; polyhedra; cubic close packing; emergent entropic forces

1. Introduction

Crystallisation is a fundamental and important process that is ubiquitous across many fields. Beyond the obvious relevance to chemistry and materials science, examples include biology (in proteins) [1], pharmaceuticals [2], manufacturing (e.g. silicon monocrystals) [3], geology (e.g. the solidification of magma) [4], and meteorology [5, 6]. While many ongoing efforts are leading to continuous advances in the field, our understanding of crystallisation at the microscopic level remains incomplete and many of its aspects remain to be explored. For this reason, simple models, like the hard sphere model, that permit the detailed study of crystallisation pathways have an important role to play in advancing our understanding of how crystals form. Hard shapes in particular serve as model systems for nanoparticle assemblies, which are the subject of intense investigations for numerous applications [7, 8], e.g. photonic materials [9],

CONTACT Sharon C. Glotzer sglotzer@umich.edu
*These authors contributed equally to this work.

Supplemental data for this article can be accessed here. https://doi.org/10.1080/00268976.2019.1668574

plasmonics [10, 11], drug delivery [12], catalysis [13], or sensing [14].

Dense systems of hard spheres crystallise into the cubic close-packed sphere packing (*ccp*, also termed *fcc* for its face-centred cubic Bravais lattice), due solely to entropy maximisation. This counterintuitive fact has been known since pioneering computer simulations in the late 1950s [15, 16]. Likewise, dense systems of hard polyhedra spontaneously self-assemble into ordered, equilibrium colloidal crystals, again to maximise entropy [17–23]. Of the many crystal structures discovered or predicted to date, the large majority are *ccp* with respect to the particle centroids. While it is not surprising that spheroidal polyhedra might self-assemble the *ccp* crystal phase, highly faceted shapes can also form *ccp* crystals. The most obvious of these is the rhombic dodecahedron (RHD), which has the shape of the Voronoi cell of *ccp*, and thus packs into an *fcc* lattice with packing fraction $\phi = 1$ at infinite pressure [24]. Between the RHD and the sphere, however, are infinitely many, increasingly vertex-truncated (and thus 'rounder') RHD that also form *ccp* due solely to entropy maximisation. Do they all crystallise into a *ccp* structure in the same way? Are there certain shape features that make it easier – or harder – for different shapes to form *ccp*?

We know how fluids of hard spheres nucleate and grow the *ccp* crystal in Monte Carlo (MC) simulations from the pioneering work of Auer and Frenkel [25, 26] and many additional studies [27–31]. Those works serve as a baseline for our study. Thapar and Escobedo simulated three different regular hard polyhedra that each form a different crystal structure upon densification [32]. They found that each system crystallised into its crystal structure more easily than spheres crystallise into *ccp*; they attributed that difference to local orientational order in the dense fluid phases that is commensurate with local order in the respective crystal. This similarity between fluid and crystal local structure has long been argued to lower the nucleation barrier between fluid and crystal [33]. The similarity of local structure in hard-polyhedron fluids and their crystals was also reported in a 2012 study of 145 different polyhedra, which showed that the existence of a crystal structure could consistently be anticipated by knowing only the local structure in the dense fluid and the shape's asphericity as measured by the isoperimetric quotient [34]. More recently, machine learning has been brought to bear on this problem, resulting in the discovery of two independent shape measures able to predict the crystal structure a shape is likely to self-assemble into with over 95% probability, provided the structure is among one of many in the training dataset [35].

All of these hard-particle systems are purely athermal, and therefore all contributions to the free energy are entropic: when the crystal state has more microstates available to it than the fluid phase at the same density, the crystal will be the stable equilibrium phase. For polyhedral shapes, alignment of the facets tends to increase the number of available microstates compared to disordered arrangements, contributing to crystallisation. This tendency towards local particle alignment is the result of many-body, statistical considerations, which can be quantified by potentials of mean force and torque (PMFTs) [36, 37]. Importantly, the PMFT expresses – in units of free energy – the multi-body nature of the effective interactions in an entropic system in terms of pairwise quantities that can be easily calculated in simulation, in the dense fluid as well as in the crystal phase [37]. Local variations in the PMFT reflect variations in the effective strength and directionality of the directional entropic forces (DEFs) between neighbouring particles. DEFs indicate weak local ordering in dense fluid phases that precede crystallisation, in agreement with prior work (using a different quantity) by Thapar and Escobedo [32]. Details on the calculation of PMFT and DEF – which is carried out independent of particle shape and thermodynamic phase – may be found in Refs. [36, 37], and in the Supplementary Information (SI).

The rhombic dodecahedron, as the Voronoi polyhedron of *ccp*, has its large facets aligned with interparticle contacts, and thus has strong entropic forces driving it towards *ccp*. Thus we expect the RHD to form *ccp*. If the vertices of the rhombic dodecahedron are truncated – gradually changing the shape into a rhombicuboctahedron – the original facets shrink and new, competing facets with their own associated DEFs are introduced. This transformation should lead to a decrease in strength of the original, *ccp*-forming DEFs. We hypothesise that this decrease should result in an increased free energy barrier to nucleation of the crystal; the aim of this paper is to test this hypothesis.

2. Model and methods

We compare the sphere (with isoperimetric quotient $IQ = 1$; Figure 1(a,b) and defined in the SI) with an interpolation series of polyhedra between the rhombic dodecahedron ($IQ = 0.74$; Figure 1(c,d)) and rhombicuboctahedron ($IQ = 0.87$) *via* vertex truncation t from 0 to 1, respectively. This interpolation produces a homologous series of shapes, all sharing the same symmetry and all forming *ccp* (see Figure 2(a)). The six polyhedra we investigated have $t = 0$, 0.2, 0.4, 0.6, 0.8, and 1.0, and represent a subset of the 423-family of shapes whose putative densest packings were reported by Chen

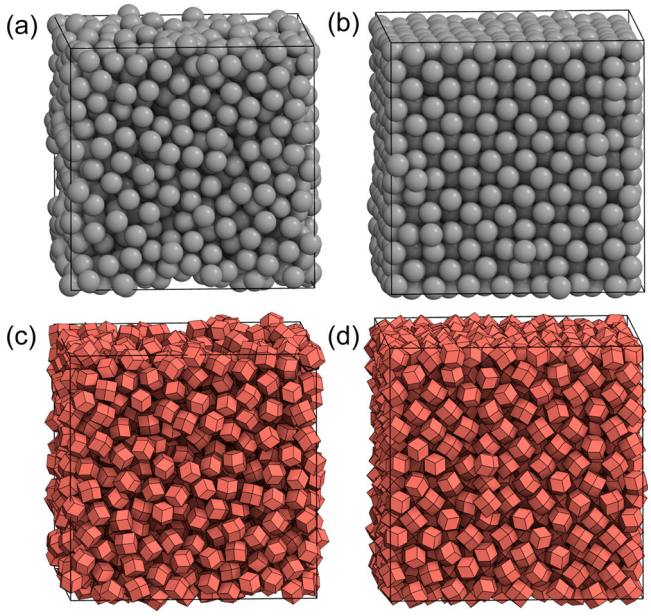

Figure 1. Simulated fluids of spheres (a) and rhombic dodecahedra (c), alongside crystals for each (b,d). Simulations were performed at $|\Delta\mu| = 0.4$ between the fluids and solids. For illustration purposes here we show only $N = 1372$ particles.

et al. [38] and whose assemblies were reported by Klotsa *et al.* [39]. In their notation, our truncation between the rhombic dodecahedron and rhombicuboctahedron follows the parameters $a = 2 - (2 - \sqrt{2})t$, $b = 2$, $c = 3 - (\sqrt{2} - 1)t$. These parameters describe the distance of sets of planes with different symmetry, with decreasing a corresponding to a set of planes perpendicular to the 4-fold axes moving inwards (truncating the 4-fold vertices of the rhombic dodecahedron) and decreasing c corresponding to planes perpendicular to the 3-fold axes moving inwards (truncating the 3-fold vertices). Additional details are provided in the SI.

This family of shapes has the added benefit that it is experimentally realisable, e.g. synthesis methods exist to form these polyhedra at the colloidal scale by etching crystalline gold rhombic dodecahedra [40]. We predict differences in the different shapes' assembly pathways by quantifying the DEFs *via* the PMFT method of van Anders *et al.* [36, 37]; the PMFT quantifies the anisotropic nature of the multi-body interactions that give rise to DEFs. We then measure these differences in the crystallisation behaviour of RHD and the other nearby shapes in the series compared to spheres. We compare fluids of different shapes at the same chemical potential difference, $|\Delta\mu|$. The chemical potential difference represents the Gibbs free energy per particle for transitioning from one phase to the other and thus corresponds to the thermodynamic driving force for crystallisation. Importantly, we purposely do not consider nor test classical nucleation theory; instead, we compare quantities that in this respect are model-free.

We performed hard particle Monte Carlo simulations using HPMC [41], a plugin to the HOOMD-blue molecular dynamics package [42]. From these simulations, we calculated the equations of state and cluster size distributions in the region of metastability, above the fluid-crystal coexistence pressure, but close enough so that nucleation is a rare event; examples are illustrated in Figure S3 in the SI. To make fair comparisons of the nucleation behaviour, we compared the shapes at the same driving forces to crystallisation (i.e. at constant $|\Delta\mu|$). These driving forces were computed using thermodynamic integration of the equations of state,

$$\Delta\mu = \int_{P_{coex}}^{P} \left(\frac{V_{\text{crystal}}}{N} - \frac{V_{\text{fluid}}}{N} \right) \mathrm{d}P' \qquad (1)$$

(see SI), which holds for hard particle systems. This integral requires coexistence pressures for each shape (where $\Delta\mu = 0$), which we determined using the method of interfacial pinning [43, 44]. We used system sizes of $N = 3375$ $(=15^3)$ particles for the umbrella sampling simulations and of $N = 2744$ for interfacial pinning, both of which are described in detail below. All shapes are scaled to unit volume, $v_p = 1$, for simplicity when working with dimensionless pressures $\beta P v_p$. The simulations were performed in the NVT ensemble, which facilitates comparison of DEFs across systems of different shapes.

The potential of mean force and torque (PMFT) quantifies the effective directional entropic forces driving particles to align in a preferentially facet-to-facet manner in both the disordered fluid and solid phases [36, 37]. We use PMFTs to elucidate how truncation alters the local neighbourhoods for the polyhedra studied. To calculate the PMFTs, local bond environments around particles are rotated with respect to the reference particle orientation and binned, with 100 bins/dimension, on a cubic grid spanning $L_i \pm 2.5$ around particles of unit volume. PMFTs for all polyhedra were computed for fluid and solid phases at $|\Delta\mu| = 0.4$ using 4000 uncorrelated simulation frames with $N = 2048$ particles each.

The formation of clusters in the homogeneous nucleation regime is rare and without biasing methods adequate statistics cannot be obtained to achieve sufficient precision to calculate free energies. We use the well-established technique of umbrella sampling to help sample adequate statistics of the cluster size distribution [26,45]. In this approach, a harmonic bias potential (called 'umbrella', after the potential shape) is added to the simulation to allow for sampling near a particular value of an order parameter. Here we use N_{max}, the size of the largest cluster of neighbouring particles with similar 3D local environments in the simulation, as the

order parameter for umbrella sampling simulations, and bias towards a target size N_{target} by adding the harmonic biasing potential

$$U_{\text{bias}} = k(N_{\max} - N_{\text{target}})^2. \tag{2}$$

In practice, umbrella sampling was performed by running short Monte Carlo trajectories (25 MC cycles) on the system. Measurements of the cluster size were taken after each trajectory, and Equation (2) was used to calculate ΔU to accept or reject the trial trajectory. The application of this bias energy to the system allows us to accurately sample the probability of cluster sizes occurring around different values of N_{target} in this umbrella ensemble. The statistics gathered in this biased ensemble of the counts of clusters of size $N_{\max}$, denoted C_N, are subsequently corrected to describe the original *NPT* ensemble *via* re-weighting the sampled states by the inverse of the bias energy,

$$\langle C_N \rangle = \frac{\sum_i^M C_N \, \mathrm{e}^{\beta U_{\text{bias},i}(N_{\max})}}{\sum_i^M \mathrm{e}^{\beta U_{\text{bias},i}(N_{\max})}}, \tag{3}$$

where the sum is performed over the taken samples. This re-weighting of states by the inverse energy cancels out the artificial umbrella energy that was added to the Hamiltonian. From this we can calculate accurate information about the probability distribution of the clusters of different sizes $N_{\max}$ near N_{target} in this biased ensemble and then compute free energies from $\beta F = -\ln P$, with pressure P. Free energy curves for each sampled target N_{target} are aligned to form a single contiguous curve using the weighted histogram analysis method (WHAM) [46].

The use of the largest cluster size $N_{\max}$ as the measure of order in the system is only valid when clusters of size $N_{\max}$ are rare [26, 47]. For common small clusters where this assumption is invalid, the cluster size probability distribution is sampled directly (without umbrella sampling) from simulations of the metastable fluid. In this work, we use bias potentials with $k = 0.1$ at $N_{\text{target}} = 15, 17, 20, 25, 30$ with windows spaced by 10 thereafter. Ten replicas were run of each window and combined to make the reported free energy curves, and each run equilibrates its own nucleus from a disordered fluid. Error bars for the cluster sizes and free energy maxima were calculated by bootstrap resampling on the data sets generated, performed at the level of the ten independent replica simulations and then incorporated into WHAM. Error bars are shown as the standard deviation of the results.

Interfacial pinning is used to determine coexistence pressures that are in turn used to calculate chemical potentials using thermodynamic integration [43, 44]. This method runs a two-phase simulation that holds a fluid and solid in an elongated box. A harmonic potential is applied to the system that attempts to force the stability of the phase coexistence to be half fluid and half solid in a manner similar to the umbrella sampling described previously. A two-phase simulation is constructed so that the two phases, fluid and solid, coexist along the z-axis, and such that the box dimensions in the x-y-plane are appropriate for an equilibrated crystal at the given pressure. In the two-phase *NPT* simulation, only the box length L_z is allowed to vary. Because the interfaces span the box with constant L_x and L_y, changes in the amount of fluid and solid do not alter the interfacial area or energy as long as the system remains two-phase. For each shape, several simulations are performed at different pressures. The coexistence pressure is determined by finding the pressure at which the mean applied bias energy is zero. To track the crystal, we use the same order parameter identifying crystalline particles as used in the umbrella sampling simulations.

Determining free energy barriers for cluster size formation requires a robust order parameter for tracking nucleus sizes; we used the method of ten Wolde [48] to track clusters. In the first step, we define the local bond orientational order q_{lm} for each particle i as

$$q_{lm}(i) = \sum_{j=1}^{N_n(i)} Y_{lm}(\theta_{ij}, \phi_{ij}), \tag{4}$$

where N_n of i is the number of neighbouring particles j within a cutoff distance r_{cut} of particle i, Y_{lm} is a spherical harmonic computed of the orientation of the interparticle vector r_{ij}. The bond orientational order parameter measures the local environment of each particle. To identify crystalline regions, the real component of a scalar product between all pairs of local environments is used as a measure of correlation:

$$q_l(i,j) = \Re \left(\sum_{m=-l}^{l} q_{lm}(i) q_{lm}^*(j) \right). \tag{5}$$

It is expected that the local environments in the crystal have more coherent products than the disordered fluid. In Equation (5), we do not normalise the sum, as the magnitude is a reflection of the quality of the match and indicative to some extent of the number of neighbours. For particles correlating sufficiently, we define solid-like bonds if the values of $q_l(i,j)$ exceed a certain threshold cutoff q_c,

$$S(i) = \sum_{j=1}^{N_n} H(q_l(i,j) - q_c). \tag{6}$$

Particles that possess sufficient numbers of solid-like bonds S – i.e. greater than or equal to another cutoff s_c

– are considered to be in a crystalline local environment and are eligible for particle clustering by local distance to locate crystalline clusters. For the unit-volume shapes studied here we identify the solid using $l = 6$, $r_{cut} = 1.7$, $q_c = 20$, and $s_c = 6$, which we find to work well for identifying *ccp* for these polyhedra. Similar values were previously used to study hard spheres [25, 26, 30, 32].

We also examine estimates for each shape of the critical nucleus sizes N^*, the cluster size at which $\beta\Delta G$ is maximal. The measurements of cluster sizes are noisy, because the sampled free energy barriers are broad near the peak, but overall trends remain visible. These values of N^* should be considered estimates: the exact cluster sizes are sensitive to the given cutoffs of the order parameter distinguishing the solid crystal from the fluid; however, the height of the barrier is robust to choices in these cutoffs because the stability of a given nucleus does not depend precisely on the size measured [30]. All systems presented here were analysed using the same cutoffs for the order parameter and should be subject to similar size bias. The relationships between free energy barrier height and nucleus size, as well as nucleus size and driving force are plotted in Figure S2 in the SI.

3. Results and discussion

Figure 2(b) shows the PMFT of the fluid phase for all six shapes, taken as a cross-section through the particle centres perpendicular to the four-fold axis, and Figure 2(c) shows three-dimensional isosurface plots. We see isolated free energy wells for the rhombic dodecahedron, which indicate facet-to-facet alignment. The PMFTs become more isotropic as we truncate the shapes away from the RHD towards the rhombicuboctahedron. These free energy minima are reduced with increasing truncation as the original facets of the RHD shrink and new entropic minima (free energy maxima) are introduced for the additional facets that were formerly the three-fold and four-fold vertices of the rhombic dodecahedron. These new entropic minima become prevalent at the highest truncations (especially $t = 1.0$).

The PMFTs of the crystalline phase shown in Figure 2(d,e) indicate that there are significant, geometrically forbidden, interstitial regions around the particles, because both the first- and second-neighbour shells are well-ordered. The orientational penalties enforced by local crystalline order diminish with increasing

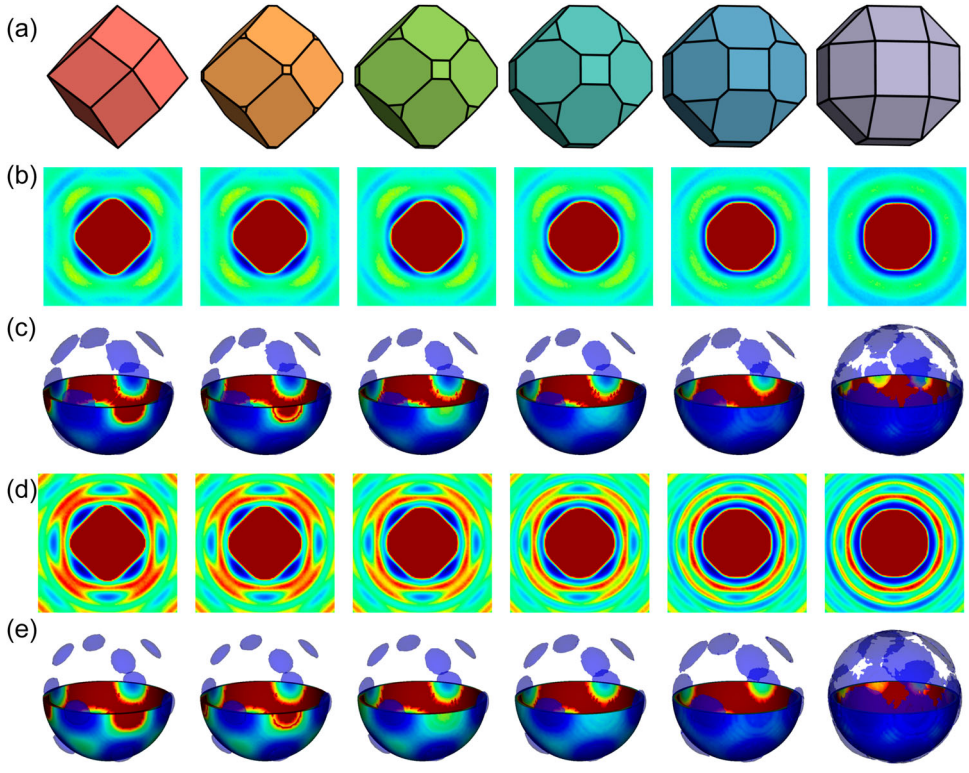

Figure 2. Potentials of mean force and torque for the (a) family of shapes between the rhombic dodecahedron and the rhombicuboctahedron (all at $|\Delta\mu| = 0.4$). (b,c) For fluids, we show cross sections through the four-fold axis (b), and three-dimensional views of the potential of mean force and torque intersecting a thin hemisphere in the first coordination shell, with iso-contours drawn at $\beta F = 0.4$ from the deepest minimum (c). For the solid phases, we show the same cross-section (d) and three-dimensional views (e). We used one consistent colour scale throughout all plots, based on a jet colour map with the maximum in the center of the plots at a value of $\beta F = 5.00$ and the minimum at a value of $\beta F = 0.00$ (see SI).

truncation: the PMFTs are much more isotropic for the rhombicuboctahedra because of lower free energy barriers to particles rotating within the crystalline phase. The penalties for being in the interstitial regions suggest the positional order corresponding to a crystal, Figure 2(d), as opposed to the fluid, Figure 2(b), but the lack of deep minima in the first coordination shell suggests that the orientation of the reference particle and its coordination shell are only weakly correlated. Misorientations of rhombicuboctahedra within the *ccp*-coordination shell carry larger entropic (smaller free energy) penalties than for the other shapes. The free energy of rotation necessary for the rhombicuboctahedra to move from one local orientational minimum to another is smaller than $\beta F = 0.4$, as indicated by the merging of the isosurfaces in the first coordination shell shown in Figure 2(e). Based on this, we predict that rhombic dodecahedra will have a smaller free energy barrier to nucleation than spheres and that this trend will also be measurable across this family of polyhedra.

In Figure 3(c), we show the free energy barriers $\beta\Delta G$, with $\beta = 1/(k_B T)$, for rhombic dodecahedra, with equivalents for the other polyhedra given in Figure S1(a–f) in the SI. Their maxima $\beta\Delta G^*$ are plotted in Figure 3(d). We observe that at a given driving force $|\Delta\mu|$, rhombic dodecahedra indeed have the smallest free energy barrier and thus nucleate the *ccp* crystal more easily than the other shapes. This is a trend across the family of polyhedra: increasing truncations away from the RHD increase roundedness, and increase the nucleation barriers at similar driving force towards the behaviour of hard spheres. The nucleation barriers are important for controlling homogeneous nucleation because the likelihood of forming a critical nucleus is proportional to $e^{-\beta\Delta G^*}$ [25, 29, 49].

As shown in Figure 3(e), the 'rounder' polyhedra exhibit notably larger driving forces to crystallise than the less truncated, more RHD-like shapes at any given pressure. The chemical potential curves for each shape appear almost linear in unitless pressure $\beta P v_p$ and are

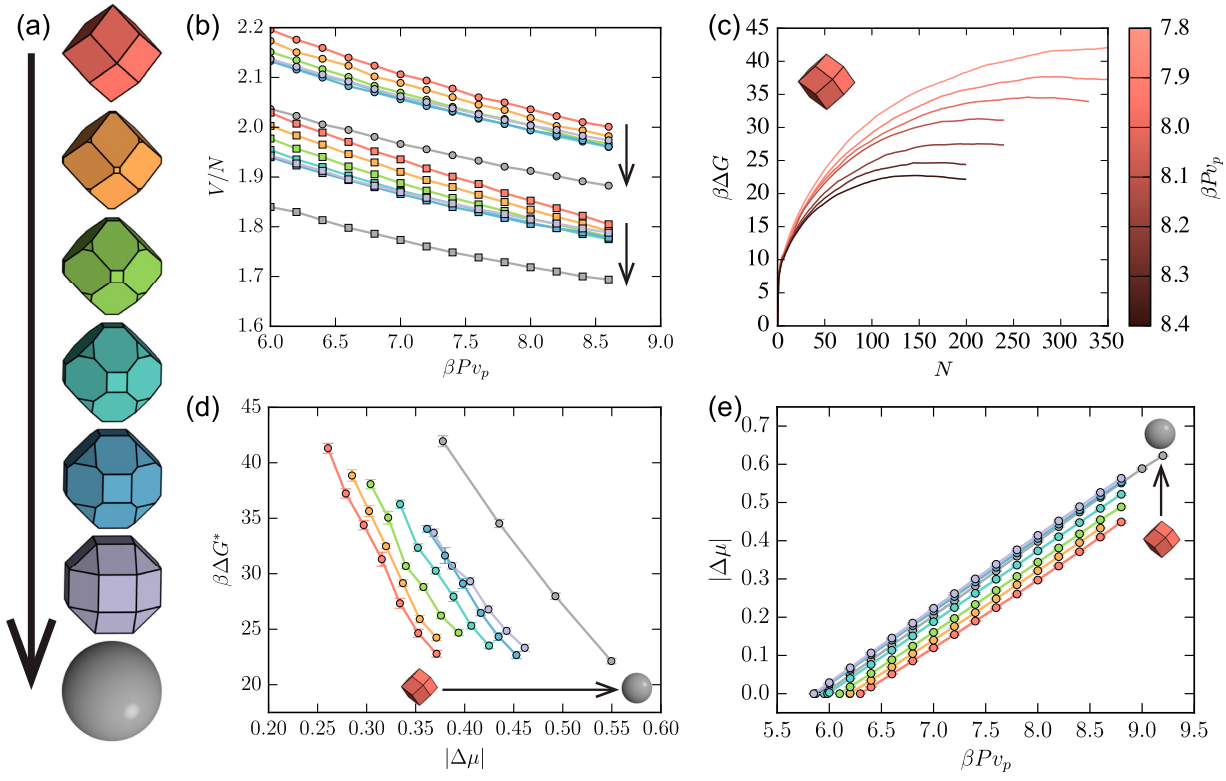

Figure 3. (a) The family of polyhedra from the rhombic dodecahedron to the rhombicuboctahedron, as well as the hard sphere. The colours of curves in all plots correspond to the colours of these shapes. (b) Equations of state expressed as free volume per particle (V/N), at various dimensionless pressures $\beta P v_p$, where v_p is the particle volume ($v_p = 1$ for all shapes). Square symbols correspond to the *ccp* crystal, and circular symbols to the fluid. Plotting in these units is useful for computing the chemical potential difference between fluid and solid phases shown in (e). (c) Umbrella-sampled Gibbs free energy barriers to crystallisation as a function of nucleus cluster size N for rhombic dodecahedra at various pressures. (d) Free energy barrier maxima βG^* for all shapes, expressed as a function of driving force $|\Delta\mu|$. Arrows in (b), (d), and (e) indicate increasing isoperimetric quotients IQ (i.e. increasing truncations of the rhombic dodecahedron $t \in \{0, 0.2, 0.4, 0.6, 0.8, 1\}$ toward the rhombicuboctahedron, followed by the sphere).

mostly spaced by their coexistence pressures. This linearity arises because the density difference between fluid and solid remains nearly constant over the modest pressure range where the fluid is metastable and measurable, and this density difference is similar for most shapes. Rhombic dodecahedra, because they can fill space, compress more in the solid than the other shapes (which manifests in the chemical potential curving slightly upwards at higher pressures), however, this effect is marginal at the investigated densities, far from the dense packing limit. Curiously, hard spheres have an intermediate coexistence pressure and chemical potential with respect to the polyhedra family (falling between polyhedra with truncations $t = 0.8$ and $t = 1$, see Figure 3(e)).

The behaviour of the DEFs as quantified by the PMFTs predicts that the local order in the fluid *vs.* the crystal should be more similar for more faceted shapes. To quantify this prediction, we characterise the probability distribution of solid-like clusters appearing in the metastable fluid prior to crystallisation. We present results in Figure 4 for the two extreme cases, rhombic dodecahedra and spheres, where we show the probabilities to find clusters of different sizes in their fluids approaching crystallisation. These values allow for a comparison of the pre-nucleation behaviour in the two fluids. At small $|\Delta\mu|$, small clusters are more common in fluids of spheres than in fluids of rhombic dodecahedra, but trends change with increasing $|\Delta\mu|$. The dearth of small clusters in the fluid of rhombic dodecahedra is likely a consequence of the lower packing fraction at small values of $|\Delta\mu|$. There is a crossover at $|\Delta\mu| > 0.25$ where larger clusters become more prevalent for rhombic dodecahedra than for spheres. A sharp increase in the number of larger clusters occurs for the fluid of rhombic dodecahedra near $|\Delta\mu| > 0.4$. This behaviour leads us to consider these larger clusters as pre-critical nuclei, which are stabilised preferentially by the strong DEFs for RHD as compared to spheres.

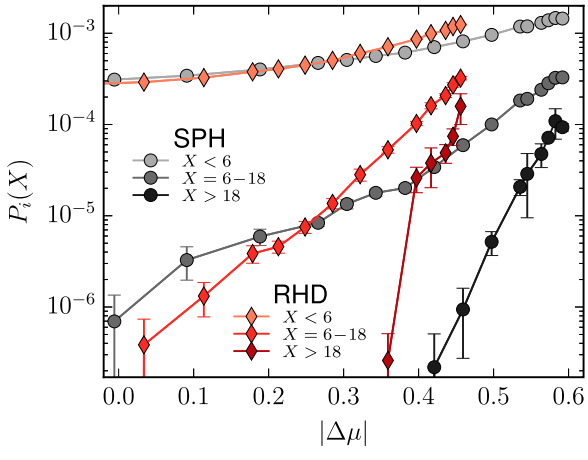

Figure 4. Probabilities of finding small (< 6 particles), medium (6–18 particles), and large (> 18 particles) clusters in equilibrated metastable fluids of spheres and rhombic dodecahedra, as a function of $|\Delta\mu|$ (see SI for details).

4. Conclusions

We showed how the nucleation barriers to entropically driven crystallisation in a family of hard polyhedra are affected by shape. We showed that truncations (leading to rounding) of the rhombic dodecahedron, the Voronoi particle of the cubic close packing, lead to increased free energy barriers to crystallisation at equivalent driving forces. Because the driving forces required for the rhombic dodecahedron to nucleate are smallest among those studied, we can surmise that the interfacial free energy terms between the fluid and solid phases must be lower for the more strongly faceted shapes in this series (i.e. towards the rhombic dodecahedron). We showed that these smaller driving forces arise from emergent entropic forces between particles that encourage facet-to-facet alignment in the fluid as characterised by potentials of mean force and torque. The additional facets formed upon truncating the rhombic dodecahedron add a level of competition between weaker directional entropic forces that hinders nucleation until higher driving forces can overcome the mismatch of local ordering between the fluid and crystal phases. We expect our findings to generalise to other shape families and to provide guidance in nanoparticle design. Recent work shows that hard shapes can sometimes crystallise from dense fluids into complex crystals with large unit cells along entropic pathways that involve multiple steps, including a fluid-fluid transition preceding crystallisation [50]. In this work, all of the crystals formed *via* a one-step nucleation and growth process. How the multistep nature of crystallisation varies with systematic changes in particle shape is the subject of ongoing work.

Acknowledgments

The authors thank Joshua A. Anderson and M. Eric Irrgang for their extensive work on HPMC for HOOMD-blue, Michael Engel for discussions on umbrella sampling, Greg van Anders for discussion of PMFTs, and Benjamin A. Schultz for help with compute resources. R. S. N., S. N., J. D., and S. C. G. designed research; R. S. N. and S. N. performed simulation and analysis; J. D. and S. C. G. supervised research; R. S. N., S. N., J. D., and S. C. G. analysed data and wrote the paper.

Disclosure statement

No potential conflict of interest was reported by the authors.

Funding

This material is based upon work supported by the National Science Foundation, Division of Materials Research Award # DMR 1409620, and by a Simons Investigator award from the Simons Foundation to Sharon Glotzer. S. N. was also supported by the U.S. National Science Foundation Open Data IGERT, DGE 0903629. J. D. acknowledges support through the Early Postdoc.Mobility Fellowship from the Swiss National Science Foundation, [grant number P2EZP2_152128]. This work used the Extreme Science and Engineering Discovery Environment (XSEDE), which is supported by National Science Foundation [grant number ACI-1053575]; XSEDE award DMR 140129. Additional computational resources and services were provided by Advanced Research Computing at the University of Michigan, Ann Arbor.

References

[1] J.P. Doye and W.C. Poon, Curr. Opin. Colloid Interface Sci. **11** (1), 40–46 (2006).
[2] J. Chen, B. Sarma, J.M.B. Evans and A.S. Myerson, Cryst. Growth Des. **11** (4), 887–895 (2011).
[3] P. Siffert and E. Krimmel, editors, *Silicon: Evolution and Future of a Technology* (Springer, Berlin, 2004).
[4] M. Wilson, *Igneous Petrogenesis: A Global Tectonic Approach* (Springer, Dordrecht, 1989).
[5] S.C. Mossop, Bull. Amer. Meteor. Soc. **66** (3), 264–273 (1985).
[6] A. Tabazadeh, Y.S. Djikaev and H. Reiss, Proc. Natl. Acad. Sci. **99** (25), 15873–15878 (2002).
[7] K. Thorkelsson, P. Bai and T. Xu, Nano Today **10** (1), 48–66 (2015).
[8] S.K. Kumar, G. Kumaraswamy, B.L.V. Prasad, R. Bandyopadhyaya, S. Granick, O. Gang, V.N. Manoharan, D. Frenkel and N.A. Kotov, Curr. Sci. **112** (8), 1635–1641 (2017).
[9] H. Zheng and S. Ravaine, Crystals **6** (5), 54 (2016).
[10] P.P. Patra, R. Chikkaraddy, S. Thampi, R.P.N. Tripathi and G.V.P. Kumar, Faraday Discuss. **186**, 95–106 (2016).
[11] G.K. Laxminarayana, M. Rozin, S. Smith and A.R. Tao, Faraday Discuss. **186**, 489–502 (2016).
[12] J. Guo, B.L. Tardy, A.J. Christofferson, Y. Dai, J.J. Richardson, W. Zhu, M. Hu, Y. Ju, J. Cui, R.R. Dagastine, I. Yarovsky and F. Caruso, Nat. Nanotechnol. **11** (12), 1105–1111 (2016).
[13] S. Guo and S. Sun, J. Am. Chem. Soc. **134** (5), 2492–2495 (2012), PMID: 22279956.
[14] M.P. Cecchini, V.A. Turek, J. Paget, A.A. Kornyshev and J.B. Edel, Nat. Mater. **12** (2), 165–171 (2013).
[15] B.J. Alder and T.E. Wainright, J. Chem. Phys. **27**, 1208–1209 (1957).
[16] W.W. Wood and T.D. Jacobson, J. Chem. Phys. **27**, 1207–1208 (1957).
[17] J. Henzie, M. Grünwald, A. Widmer-Cooper, P.L. Geissler and P. Yang, Nat. Mater. **11** (2), 131–137 (2012).
[18] P.F. Damasceno, M. Engel and S.C. Glotzer, ACS Nano **6** (1), 609–614 (2012).
[19] F. Smallenburg, L. Filion, M. Marechal and M. Dijkstra, Proc. Natl. Acad. Sci. **109** (44), 17886–17890 (2012).
[20] M. Marechal and H. Löwen, Phys. Rev. Lett. **110** (13), 137801 (2013).
[21] C.W. Liao, Y.S. Lin, K. Chanda, Y.F. Song and M.H. Huang, J. Am. Chem. Soc. **135** (7), 2684–2693 (2013).
[22] H.R. Vutukuri, F. Smallenburg, S. Badaire, A. Imhof, M. Dijkstra and A. van Blaaderen, Soft Matter **10**, 9110–9119 (2014).
[23] B.A. Schultz, P.F. Damasceno, M. Engel and S.C. Glotzer, ACS Nano **9** (3), 2336–2344 (2015).
[24] R.K. Cersonsky, G. van Anders, P.M. Dodd and S.C. Glotzer, Proc. Natl. Acad. Sci. **115** (7), 1439–1444 (2018).
[25] S. Auer and D. Frenkel, Nature **409** (6823), 1020–1023 (2001).
[26] S. Auer and D. Frenkel, J. Chem. Phys. **120** (6), 3015–3029 (2004).
[27] T. Palberg, J. Phys. **11** (28), R323–R360 (1999).
[28] P.N. Pusey, E. Zaccarelli, C. Valeriani, E. Sanz, W.C.K. Poon and M.E. Cates, Philos. Trans. R. Soc. Lond. A **367** (1909), 4993–5011 (2009).
[29] T. Kawasaki and H. Tanaka, Proc. Natl. Acad. Sci. **107** (32), 14036–14041 (2010).
[30] L. Filion, M. Hermes, R. Ni and M. Dijkstra, J. Chem. Phys. **133** (24), 244115 (2010).
[31] J. Taffs, S.R. Williams, H. Tanaka and C.P. Royall, Soft Matter **9**, 297–305 (2013).
[32] V. Thapar and F.A. Escobedo, Phys. Rev. Lett. **112** (January), 048301 (2014).
[33] F.C. Frank, Proc. R. Soc. Lond. Ser. A **215** (1120), 43–46 (1952).
[34] P.F. Damasceno, M. Engel and S.C. Glotzer, Science **337** (6093), 453–457 (2012).
[35] Y. Geng, G. van Anders and S.C. Glotzer, arXiv:1801.06219 (2018).
[36] G. van Anders, N.K. Ahmed, R. Smith, M. Engel and S.C. Glotzer, ACS Nano **8** (1), 931–940 (2014).
[37] G. van Anders, D. Klotsa, N.K. Ahmed, M. Engel and S.C. Glotzer, Proc. Natl. Acad. Sci. **111** (45), E4812–E4821 (2014).
[38] E.R. Chen, D. Klotsa, M. Engel, P.F. Damasceno and S.C. Glotzer, Phys. Rev. X **4**, 011024 (2014).
[39] D. Klotsa, E.R. Chen, M. Engel and S.C. Glotzer, Soft Matter **14**, 8692–8697 (2018).
[40] D.Y. Kim, S.H. Im, O.O. Park and Y.T. Lim, Cryst. Eng. Comm. **12** (1), 116–121 (2010).
[41] J.A. Anderson, M.E. Irrgang and S.C. Glotzer, Comput. Phys. Commun. **204**, 21–30 (2016).
[42] J.A. Anderson, C.D. Lorenz and A. Travesset, J. Comput. Phys. **227**, 5342–5359 (2008).
[43] U.R. Pedersen, J. Chem. Phys. **139** (10), 104102 (2013).
[44] V. Thapar and F.A. Escobedo, J. Chem. Phys. **141** (12), 124117 (2014).
[45] G. Torrie and J. Valleau, J. Comput. Phys. **23** (2), 187–199 (1977).
[46] A. Grossfield, *WHAM: the weighted histogram analysis method*, version 2.0.9. <http://membrane.urmc.rochester.edu/content/whamed.2013 > .
[47] S. Auer and D. Frenkel, Nature **413** (6857), 711–713 (2001).
[48] P. ten Wolde, M. Ruiz-Montero and D. Frenkel, Faraday Discuss. **104**, 93–110 (1996).
[49] M. Leocmach and H. Tanaka, Nat. Commun. **3**, 974 (2012).
[50] S. Lee, E.G. Teich, M. Engel and S.C. Glotzer, Proc. Natl. Acad. Sci. **116** (30), 14843–14851 (2019).